Effect of steel fibres on concrete behavior in 2D and 3D simulations using lattice model

J. KOZICKI, J. TEJCHMAN

Faculty of Civil and Environmental Engineering
Gdańsk University of Technology
Narutowicza 11/12
80-233 Gdańsk-Wreszcz, Poland
e-mails: jkozicki@pg.gda.pl, tejchmk@pg.gda.pl

QUASI-STATIC SIMULATIONS of a concrete behaviour with steel fibres under uniaxial tension were carried out using a discrete irregular lattice model. Fibrous concrete was described at a meso-scale as a three-phase material composed of aggregate, cement matrix, steel fibres and interfacial zones between cement matrix and aggregate, and between cement matrix and steel fibres. The effect of the fibre interface strength, fibre volume, fibre orientation, fibre length and specimen size on the concrete behaviour was investigated. The results of two- and three-dimensional analyses were compared.

Key words: aggregate, bond, cement matrix, concrete, fracture, lattice model, steel fibres, uniaxial tension.

1. Introduction

CONCRETE IS STILL THE MOST widely used construction material since it has the lowest ratio between cost and strength as compared to other available materials. However, it has two undesirable properties, namely: low tensile strength and large brittleness, that cause the collapse to occur shortly after the formation of the first crack (SOULIOTI *et al.* [31]). Therefore, the application of concrete subjected to impact, earth-quaking and fatigue loading is strongly limited. To improve these two negative properties and to achieve a partial substitute of conventional reinforcement, an addition of short discontinuous, randomly oriented fibres (steel, glass, synthetic and natural) can be practiced among others. Steel fibres are the most used in concrete applications due to economy, manufacture facilities, reinforcing effects and resistance to the environment aggressiveness. By addition of steel fibres, the following properties of plain concrete: tensile splitting strength, flexural strength, first cracking strength, toughness, stiffness, durability, impact resistance, fatigue and wear strength increase, and deflection, crack width, shrinkage and creep are reduced (SHAH and RANGAN [28], BENTUR and MINDESS [5], BALAGURU and SHAH [3], CHENKUI and GUOFAN [7], ZOLLO [38]). In turn, compressive strength can slightly increase (MOHAMMADI *et al.* [24]) or

slightly decrease (ALTUN *et al.* [2]). The addition of steel fibres aids in converting the brittle characteristics to the ductile ones. Fibres limit the formation and growth of cracks by providing pinching forces at crack tips. They bear some stress that occurs in cement matrix themselves and transfer the other portion of stress at stable cement matrix portions. Real effects of fibre addition can be observed as a result of the bridging stress offered by the fibres after the peak load. The fibre-reinforced concrete specimens develop first a pattern of fine distributed cracks, instead of directly failing in one localized crack. Fibre-reinforced concrete has found many applications in tunnel linings, wall cladding, bridge desks, pavements, slabs on grounds, factory (industrial) floors and slabs, dams, pipes, fire protection coatings, spray concretes (BALAGURU and SHAH [3], ZOLLO [38], KRSTULOVIC-OPARA *et al.* [19], FALKNER and HENKE [10], SCHNÜTGEN and TEUTSCH [30], WALRAVEN and GRÜNEWALD [36]). It can be also used for repair, rehabilitation, strengthening and retrofitting of existing concrete structures (LI *et al.* [20]).

The degree of improvement of fibrous concrete depends upon many different factors such as: size, shape, aspect ratio (ratio between length and diameter), volume fraction, orientation and surface characteristics of fibres, ratio between the fibre length and maximum aggregate size, and volume ratio between long and short fibres and concrete class (SHAH and RANGAN [28], BENTUR and MINDESS [5], BALAGURU and SHAH [3], ZOLLO [38], ALTUN *et al.* [2], MOHAMMADI *et al.* [24]). The fibre orientation depends on the specimen size and flow direction of the fresh concrete against a casting direction (REDON and CHERMANT [27]). Fibres hinder the flowability of fresh concrete that decreases the workability by increasing the pore volume resulting in strength decrease (what is visible during compression). The most suitable fractions for concrete mixes are between 0.5% and 2.0% by volume of concrete. The aspect ratios of steel fibers used in concrete mix are varied between 50 and 100. The strength and ductility of fibrous concrete beams increase both with decreasing specimen size (WARD and LI [37], LIN [22], BALENDRAN *et al.* [4]).

In spite of positive properties, fibrous concrete did not find such acknowledgment and application as usual concrete. There do not still exist consistent dimensioning rules due to the lack sufficient large-scale static and dynamic experiments, taking into account mainly the effect of the fibre orientation. There is a general lack of confidence in the design, particularly under bending in spite of existing tools on different scale. An analytical micro-scale approach has been proposed in by LIM *et al.*[23]. On the meso scale, a truss model has been used to study the material behavior (BOLANDER and SAITO [6], VAN HAUWAERT and VAN MIER [34], LI *et al.* [21]. In turn, on the macro scale, constitutive models have been developed that can be used in finite element computations (AL-TAAN and EZZADEEN [1], KOOIMAN *et al.* [14]). Recently, a numerical continuum approach was proposed by RADTKE *et al.* [25, 26], wherein the existing continuum

approach to model concrete failure was combined with a discrete representation of fibres by adding extra nodal forces at fibre ends, measured during the pull-out of a fibre from a matrix specimen. In turn, a semi-analytical method was proposed by Jones *et al.* [11] to predict the flexural behavior of steel fibres, wherein the flexural capacity of the critical section was related to five principal parameters: the uniaxial compressive stress-strain relationship, the uniaxial tensile stress-strain relationship, the single fibre pull-out load versus crack-width relationship, the number, distribution, embedment lengths and orientations of the fibres bridging the cracked section, the strain and crack-width profiles of the uncracked and cracked sections respectively in relation to the mid-span beam deflection. Kabele [12] has used a multi-scale framework for modeling of fracture in high performance fiber-reinforced cementitious composites.

This paper is focused on mechanical modeling of fibre-reinforced concrete. The calculations were carried out with a geometrical irregular linear 3D lattice model (Kozicki [15], Kozicki and Tejchman [16, 17]). In the model, individual straight steel fibres were explicitly modeled. Such explicit modeling of fibres, with their realistic stochastic distribution within concrete, allowed one for a better understanding of individual and collective effects of fibres on the concrete behaviour. Two- and three-dimensional calculations were performed with concrete considered as heterogeneous material at meso-scale, composed of aggregate inclusions, cement matrix, steel fibres, matrix-inclusion interface and matrix-fibre interface. Circularly in 2D or spherically in 3D-shaped aggregates were randomly positioned in the domain according to a granulometric distribution. Our model is composed of rigid body rod elements creating a lattice that breaks according to a simple rule. A material meso-structure is mapped onto the lattice so that each element is associated with a particular material phase or interface. Of special interest in this work is modeling of the different strength of the cement matrix-fibre interface and stochastic distribution of aggregate and fibres in 3D concrete specimens. The effect of the length of steel fibres and their orientation on the global concrete behavior during uniaxial tension was studied. In addition, a deterministic size effect was investigated.

Our irregular lattice model has been already successfully used to simulate the fracture process in two-dimensional and three-dimensional plain concrete specimens subject to uniaxial tension, uniaxial compression, three-point bending and mixed shear-extension (Kozicki and Tejchman [16, 17]). The effect of aggregate bond, aggregate density, aggregate size and specimen size on the material strength and failure was realistically captured in discrete simulations.

The numerical results in this paper were qualitatively compared with experiments only. First, it is due to the lack of the exact data on material microstructure in experiments (e.g. aggregate density, aggregate size distribution, aggregate shape, interface thickness), which is of major importance in calculations

carried out with a lattice model. Second, the aim of the paper is to show some aspects of mechanical modelling and to check a capability of our model to simulate fracture in fibrous concrete. A quantitative analysis will be carried out soon.

2. Lattice model

Our lattice model (Kozicki and Tejchman [16, 17], Kozicki and Donze [18]) differs from classical lattice beam models composed of beams connected by non-flexible nodes (van Mier *et al.* [33], Schlangen and Garboczi [29], van Mier and van Vliet [35]) in that it consists of rods with flexible nodes and longitudinal deformability, rotating as rigid bodies. Thus, shearing, bending and torsion are represented by a change of rotational angles between rod elements connected by 3 different springs (2 bending springs and 1 torsional spring) (Fig. 1a). This quasi-static model is of a kinematic type. The calculations of element displacements are carried out on the basis of the consideration of successive geometrical changes of rods due to translation, rotation, normal bending and torsional deformation. Thus, the global stiffness matrix is not built and the calculation method has a purely explicit character. In spite of necessity of the application of small displacement increments (what is the inherent property of explicit numerical procedures), the computation time is significantly reduced as compared to implicit lattice model solutions (Schlangen and Garboczi [29], van Mier and van Vliet [35]).

In the model, the quasi-brittle material was discretized in the form of a tetrahedral (3D simulations) or a triangular (2D simulations) grid of lines. The lattice topology was defined by the Delaunay tessellation of an irregular set of nodal points (thus the distribution of rod elements was assumed to be completely random). First, a tetrahedral (or triangular) grid of nodes was created in the material with the side dimension equal to g. Then each node was displaced by a vector of a random direction and a random magnitude smaller than s. The nodes randomized in this way were connected with each other, and each edge in the mesh formed a lattice. Thus, the model needs 2 grid parameters (g and s) only to randomly distribute rods in the lattice. In the calculations, we assumed $g = 1$ mm (2D calculations) or $g = 2$ mm (3D calculations) and $s = 0.6g$. A uniform regular tetrahedral (or triangular) mesh can be obtained with $s = 0$. The rods possessed longitudinal stiffness described by the parameter k_l (controlling the rod length change) and the nodal springs possessed the bending stiffness described by the parameter k_b controlling the change of the bending angle α_1 (α_1 – rotational angle around the axis Z in the plane XY which is formed by two rods 'i' and 'j') (Fig. 1b). In 3D calculations, the nodal springs had also the torsional stiffness described by the parameter k_t controlling the change of the angles α_2 and α_3; α_2 – rotational angle of the rod 'j' around the axis of the
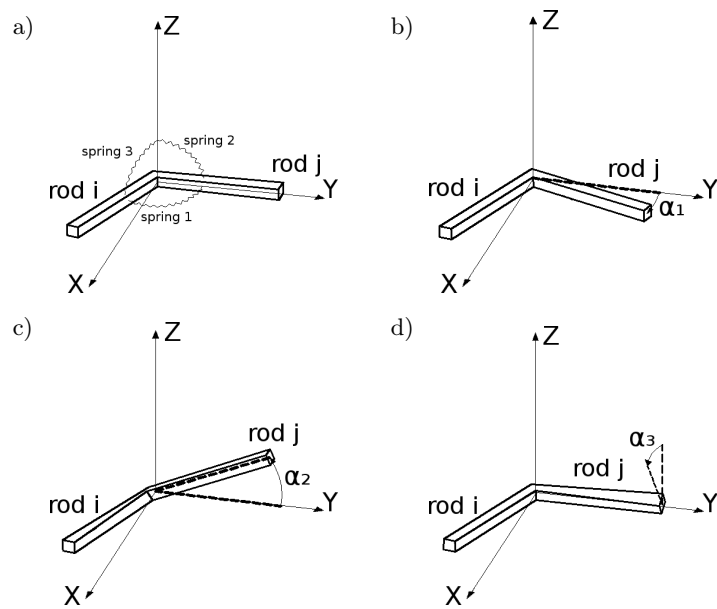
Fig. 1. Lattice rods connected by two bending and one torsional springs: a) initial position, b) bending angle $\alpha 1$, c) rotational angle α_2, d) rotational angle α_3 (Kozicki [15]).

rod 'i' (which is the rotational axis of the spring '2') and α_3 – rotational angle of the rod 'j' around its own axis (which is the rotational axis of the spring '3') (Figs. 1c and 1d). Thus, the spring '2' caused torsion of the rod 'i' and bending of the rod 'j' and the spring '3' caused torsion of the rod 'j' and bending of the rod 'i'. Thus, each rod pair had separately two bending springs and one torsional spring. The displacement of the center of each rod element was calculated as the average displacement of its two end nodes from the previous iteration step (Kozicki and Tejchman [16])

$$(2.1) \qquad {}_i\Delta \mathbf{X} = \frac{{}_i^A\Delta\mathbf{X} + {}_i^B\Delta\mathbf{X}}{2},$$

where ${}^A\Delta\mathbf{X}$ and ${}^B\Delta\mathbf{X}$ – displacement of the end nodes A and B in the rod element i, respectively. The displacement vector of each element node was obtained by averaging the displacements of the end of elements attached to this node caused by translation, rotation, normal, bending and torsional deformation

$$(2.2) \qquad {}^j\Delta\mathbf{X} = \sum_i \frac{{}_i\Delta\mathbf{W} + {}_i\Delta\mathbf{R}}{{}^j n_{\text{sum}}} + \frac{\displaystyle\sum_i \frac{1}{{}_i d_{\text{init}}}({}_i\Delta\mathbf{D}_i k_l + {}_i\Delta\mathbf{B}_i k_b + {}_i\Delta\mathbf{T}_i k_t)}{\displaystyle\sum_i \frac{1}{{}_i d_{\text{init}}}({}_i k_l + {}_i k_b + {}_i k_t)},$$

wherein: ${}_i\Delta\mathbf{X}$ – resultant node displacement, ${}_i\Delta\mathbf{W}$ – node displacement due to the rod translation, ${}_i\Delta\mathbf{R}$ – node displacement due to the rod rotation, ${}_i\Delta\mathbf{D}$ –
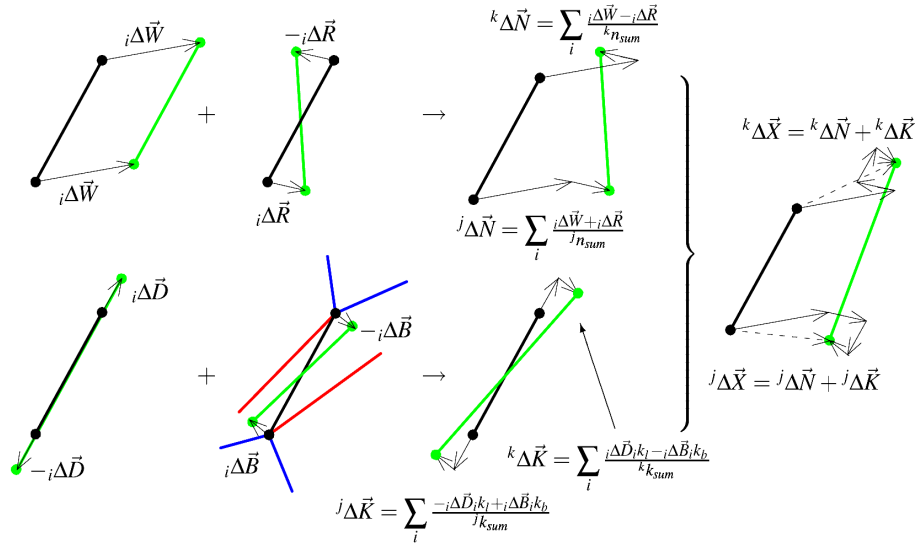
Fig. 2. General scheme to calculate displacements of rod elements in 2D lattice (Kozicki and Tejchman [16]).

node displacement due to a change of the rod length (controlled by k_l), $_i\Delta\mathbf{B}$ – node displacement due to a change of the bending angle between two neighboring rods (controlled by k_b), $_i\Delta\mathbf{T}$ – node displacement due to a change of the torsional angle between two neighboring rods (controlled by k_t), i– successive rod number connected with the node, j – node number, $^j n_{\text{sum}}$ – number of rods attached to the node j and $_i d_{\text{init}}$ – initial length of the rod i. Fig. 2 shows a simplified scheme for 2D calculations of rod displacements (without torsion). The node displacements were calculated successively during each calculation step beginning first from elements along boundaries subjected to prescribed displacements. The normal strain ε, shear angle γ and bending angle χ in rods were for 2D problems equal to (Fig. 3b)

$$(2.3) \qquad \varepsilon = \frac{_i d - _i d_{\text{init}}}{_i d_{\text{init}}}, \qquad \gamma = \frac{_i\alpha_1^A + _i\alpha_1^B}{2}, \qquad \chi = \frac{_i\alpha_1^A - _i\alpha_1^B}{2},$$
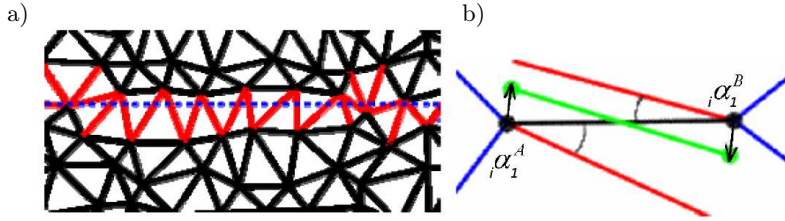
a)   b)

Fig. 3. 2D lattice: a) arbitrary cross-section, b) angles to calculate shear angle and bending angle in rods (Kozicki and Tejchman [16]).

where $_id$ and $_id_{\text{init}}$ are the current and initial length of the rod and $_i\alpha_1^A$ and $_i\alpha_1^B$ are the bending angles calculated at both ends of the rod (as cumulative values from all rods connected to both ends). The normal stress and shear stress were respectively (E – modulus of elasticity, G – shear modulus)

$$(2.4) \qquad \sigma = \varepsilon k_l E \qquad \text{and} \qquad \tau = \gamma k_b G.$$

The resultant force F in a selected specimen's cross-section area A was determined with the aid of the normal strain ε, shear strain γ, stiffness parameters k_l, k_b and k_t, modulus of elasticity E, shear modulus G and specimen's cross-section area A

$$(2.5) \qquad F = A\sum (\varepsilon k_l E + \gamma k_b G),$$

where the sum is extended over all rods that cross a selected specimen's plane A (Fig. 3a). For the bending stiffness parameter $k_b = 0$ (Eq. (2.2)), the lattice behaved as a truss, otherwise as a frame. The rod element broke and was removed from the lattice if the corresponding local threshold (permissible) tensile strain $\varepsilon_{\min}$ was exceeded. By applying Eqs. (2.2) and (2.5), the force equilibrium was obtained in each lattice node with the accuracy of 1% (what required always about 10 iterations) and was verified by comparing the calculated resultant force along the top and at the bottom of the specimen.

All the presented numerical calculations were strain-controlled. On the basis of calculations of plain concrete (Kozicki and Tejchman [17]), the critical global strain increment expressed as

$$(2.6) \qquad \Delta\varepsilon_{\text{crit}}^{\text{gl}} = (l_r\varepsilon_{\min})/\Delta l$$

should be larger than $\Delta\varepsilon_{\text{crit}}^{\text{gl}} > 500$ in a single calculation step to obtain a negligible effect of the strain increment on numerical results of the global force (about 1–2%), where l_r – average rod length, $\varepsilon_{\min}$ – threshold local tensile strain and Δl – vertical displacement increment of the specimen edge. It means that minimum 500 iterations were required to remove a single rod. If this condition in Eq. (2.6) was not preserved, both the crack shape and crack direction could depend upon the strain increment. The ratio between the mean lattice rod length l_r and the smallest specimen size h had to be at least 1/100–1/50 ($l_r/h \leq 1/100$–$1/50$) in 2D and 1/66–1/33 ($l_r/h \leq 1/66$–$1/33$) in 3D specimens, to obtain a negligible effect (about 2%) of the rod length on stress results. Alternatively, a non-local approach could be used when applying larger rods (Kozicki and Tejchman [17]). However, it was connected with a significant increase of the computation time. Therefore, an application of smaller rods using a local approach was more efficient with respect to the computation time. The calculation algorithms were given in detail by Kozicki [12].

In the 2D and 3D discrete calculations, different properties were prescribed to lattice elements to simulate the concrete behaviour at meso-scale. The concrete
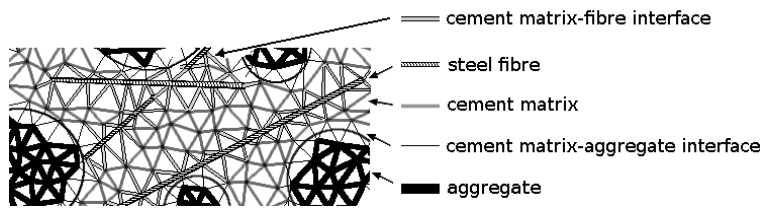
Fig. 4. 2D lattice composed of rods to simulate three phases (steel fibres, cement matrix and aggregate) and two interfaces (matrix-aggregate interface and fibre-matrix interface) in concrete at meso-scale.

was composed of aggregate, cement matrix, fibres, bond between aggregate and cement matrix and bond between fibres and cement matrix (Fig. 4, Tab. 1). The interfacial cement matrix-aggregate zones were distinguished by assigning different properties to rods which connected directly the aggregate with the cement matrix. Their width ranged from 0.3 mm to 2 mm in 2D calculations ($g = 1$ mm) and from 0.6 mm to 4 mm in 3D calculations ($g = 2$ mm). In turn, the interfacial cement matrix-fibre zones were distinguished by assigning different properties to rods which connected directly the steel fibres with the cement matrix; their width also changed between 0.3 mm–2 mm (2D model) and between 0.6 mm–4 mm (3D model). The mean aggregate diameter was assumed to be $d_{50} = 12$ mm (Fig. 5). The aggregate volume or aggregate area percentage was assumed to be 60%. The fibre volume was $V_f = 1.5\%$ in 3D simulations. In turn, the fibre area in 2D analyses was $A_f = 1.5\%$. The minimum rod length was 0.2 mm and the maximum one was 2 mm ($l_r = 1$ mm on average) in 2D calculations. In

Table 1. Material parameters used in 2D and 3D calculations of fibrous concrete at meso-scale (KOZICKI and TEJCHMAN [32]).

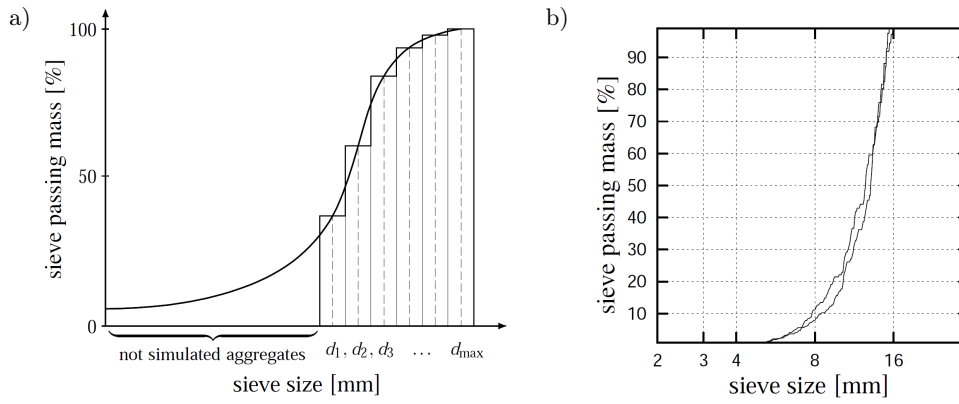| Concrete phase	Modulus	Stiffness ratio $p = k_b/k_l$ (tension)	Stiffness ratio $p = k_b/k_l$ (compression)	Stiffness parameter k_l	Threshold local tensile strain $\varepsilon_{\min}[\%]$	Fibrous interface type
Cement matrix	20	0.6	0.2	0.01	0.2	A)–D)
Aggregate inclusions	60	0.6	0.2	0.03	0.133	A)–D)
Cement matrix-aggregate interface	14	0.6	0.2	0.007	0.05	A)–D)
Cement matrix-fibre interface	20	0.6	0.2	0.01	0.2	A)
	14	0.6	0.2	0.007	0.025	B)
	14	0.6	0.2	0.007	0.05	C)
	14	0.6	0.2	0.007	0.1	D)
	14	0.6	0.2	0.007	0.5	D)
	14	0.6	0.2	0.007	1.0	D)
Steel fibres	160	0.6	0.2	0.08	90	A)–D)

Fig. 5. Aggregate sieve curve with mean particle diameter of $d_{50} = 12$ mm: a) approximation of grading curve with discrete number of aggregate sizes, b) prescribed and generated grading curve.

3D calculations, the minimum rod length was 1.2 mm and the maximum one was 4 mm ($l_r = 2$ mm on average). The size of the 3D concrete specimens was $5 \times 5 \times 5$ cm^3 or $10 \times 10 \times 10$ cm^3, respectively. In turn, the size of the 2D concrete specimens was 5×5 cm^2 and 10×10 cm^2, respectively. The number of rods was 170 000 (3D specimen $5 \times 5 \times 5$ cm^3), 1 400 000 (3D specimen $10 \times 10 \times 10$ cm^3), 8 000 (2D specimen 5×5 cm^2), 36 000 (2D specimen 10×10 cm^2), respectively. The computation time with 1 400 000 rods in 3D simulations was e.g. 90 hours on PC 3.5 GHz. A length of straight steel fibres changed between $l_f = 10$ mm and $l_f = 60$ mm. The fibre width b_f (2D simulations) or fibre diameter d_f (3D simulations) corresponded to the grid parameter g.

The material parameters of Table 1 were determined in the following way. The moduli of elasticity for aggregate, cement matrix and steel fibres can be directly measured in laboratory tests. The stiffness parameter $p = k_b/k_l$ was determined during compression to obtain a realistic Poisson's ratio for concrete (KOZICKI and TEJCHMAN [16]). We assumed the same ratio $p = k_b/k_l$ for all phases ($p = 0.2$ in compression). However, the different value of p was assumed in tension, i.e. $p = 0.6$ (Fig. 6a). The assumption of the different value of the ratio p in tension and compression was necessary to obtain a realistic crack shape during a mixed shear-extension failure mode (KOZICKI and TEJCHMAN [17]). For pure extension, a different value of the ratio p in tension and compression had no effect on the results. The chosen ratio $p = k_b/k_l$ (different in compression and tension) caused the different Poisson's ratio: $\upsilon = 0.22$ (compression) and $\upsilon = 0.07$ (tension), respectively (Fig. 6b). The latter numerical outcome has to be verified by experiments. The ratios between the parameters k_l and $\varepsilon_{\min}$ for the cement matrix and aggregate were assumed on the basis of ratios between the moduli of elasticity and tensile strengths, respectively (VAN MIER et al. [33]).
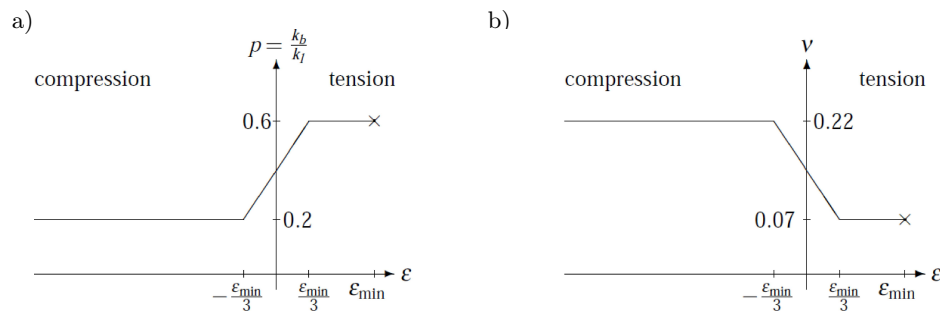
a)

$p = \frac{k_b}{k_l}$

compression   tension

0.6

0.2

$-\frac{\varepsilon_{\min}}{3}$ $\frac{\varepsilon_{\min}}{3}$ $\varepsilon_{\min}$ ε

b)

v

compression   tension

0.22

0.07

$-\frac{\varepsilon_{\min}}{3}$ $\frac{\varepsilon_{\min}}{3}$ $\varepsilon_{\min}$ ε

FIG. 6. Assumed change of ratio $p = k_b/k_l$: a) and resulting Poisson's ratio of the lattice versus threshold local strain $\varepsilon_{\min}$, b) KOZICKI and TEJCHMAN [17].

The local parameter $\varepsilon_{\min}$ for cement was chosen to obtain a realistic value of the global strain corresponding to the strength during uniaxial tension. Although the width of the interfacial transition zone between aggregate and cement matrix is only about 0.05 mm, the ITZ is commonly regarded as a weak link in determining both the mechanical and transport properties of cement-based composites.

The role of the ITZ is especially important when considering concretes where the volume fractions of inclusions are rather high, in the range 60% to 75% of the total material volume. Therefore, we also assumed that the weakest phase was bond between aggregate and cement matrix (VAN MIER et al. [33], KOZICKI and TEJCHMAN [17]). The material parameters for the interface between aggregate and cement matrix were assumed following VAN MIER et al. [33]. In calculations, the stiffness parameter k_t was always assumed as $k_t = k_b$. In the case of the cement matrix-fibre interface, the different interface strength was taken into account by changing the threshold local bond strain $\varepsilon_{\min}$ (Table 1) (with the values of E and p similar as for the aggregate interface). We considered the following 4 cases:

A) no interface between the fibres and cement matrix,
B) the strength of the cement matrix-fibre interface was smaller than the strength of the cement matrix-aggregate interface (threshold local tensile strain in the cement matrix-fibre interface was $\varepsilon_{\min} = 0.025\%$),
C) the strength of the cement matrix-fibre interface was equal to the strength of the cement matrix-aggregate interface ($\varepsilon_{\min} = 0.05\%$),
D) the strength of the cement matrix-fibre interface was greater than the strength of the cement matrix-aggregate interface ($\varepsilon_{\min} = 0.1\%$, $\varepsilon_{\min} = 0.5\%$, $\varepsilon_{\min} = 1.0\%$).

The case C) is not physically realistic; it was taken into account for purposes of numerical calculations only. The material parameters for rigid steel fibres were chosen as (Table 1): $E = 160$ GPa, $p = 0.6$ (tension) and $p = 0.2$ (compression), $k_l = 0.08$ and $\varepsilon_{\min} = 90\%$.
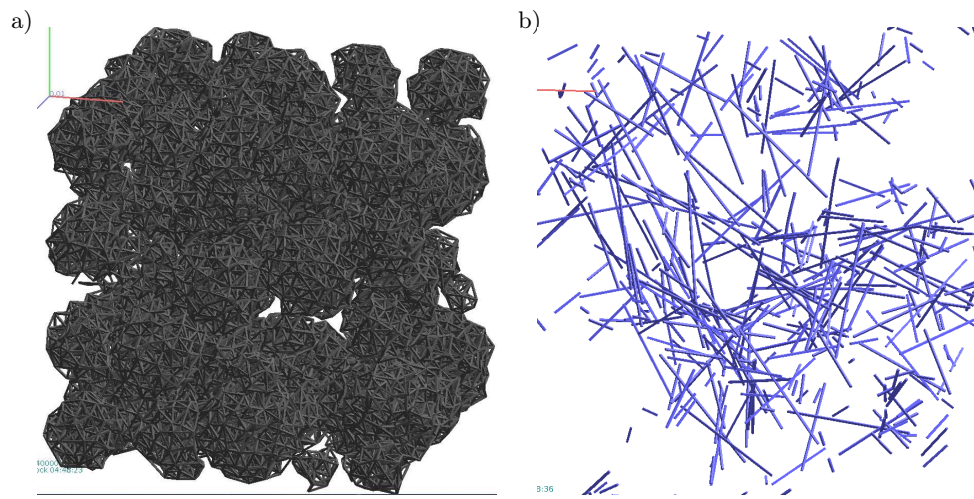
a)

b)

Fig. 7. Spatial distribution of aggregate: a) and steel fibres, b) in 3D concrete specimen $5 \times 5 \times 5$ cm^3 with 1.5% fibre volume.

An initial process of forming of a fibrous concrete specimen (Fig. 7) was the following. First, steel fibres were distributed at random positions within the specimen. Next, to obtain a distribution of fibres in the entire specimen, a so-called iterative repulsion algorithm was used. Each steel fibre was described by 20 points (it was divided into 19 equal parts). The fibre points were subjected to repulsion from other fibre points and specimen boundaries were inversely proportional to the squared distance between two points. As a result, a random distribution of fibres in the entire specimen was obtained. Next, the number of spheres with a different diameter was calculated according to Fig. 5a, to fit a prescribed granulometric curve. The spheres were inserted at random positions into a concrete specimen by ignoring the fibre and sphere overlaps. Afterwards, a repulsion procedure was again used (in which each sphere was represented by a single point), if an overlap was detected (Eq. (2.7)): sphere to sphere or sphere to fibre. This quasi-static algorithm simulated a process of sphere compaction up to the aggregate volume of 60%–70%. The size distribution of aggregate inclusions was determined using a gradation curve (Fig. 5a) (Cusatis *et al.* [8], Eckardt and Könke [9]). First, the specified numbers of particles with defined diameters were generated according to curve in Fig. 5b. Finally, the spheres describing aggregates were randomly placed in the specimen preserving the particle density and a certain mutual minimum distance (van Mier *et al.* [33])

$$(2.7) \qquad\qquad D_p > 1.1 \frac{D_1 + D_2}{2},$$

where D_p is the distance between two neighboring particle centers and D_1 and D_2 are the diameters of these two particles (sphere or fibre).

3. Numerical results

3.1. Effect of cement matrix-fibre bond strength

The results of stress-strain curves during quasi-static uniaxial tension with 2 different notched fibrous concrete specimen sizes with smooth horizontal edges, are shown in Fig. 8 (specimen 5×5 cm^2 in 2D simulations), and Fig. 9 (specimen $5 \times 5 \times 5$ cm^3 in 3D simulations), by assuming the different threshold local ensile strain $\varepsilon_{\min}$ for rods in the cement matrix-fibre interface ($\varepsilon_{\min} = 0.025\%$–$1.0\%$) (Table 1). Five stochastic simulations were performed for each strain $\varepsilon_{\min}$ with
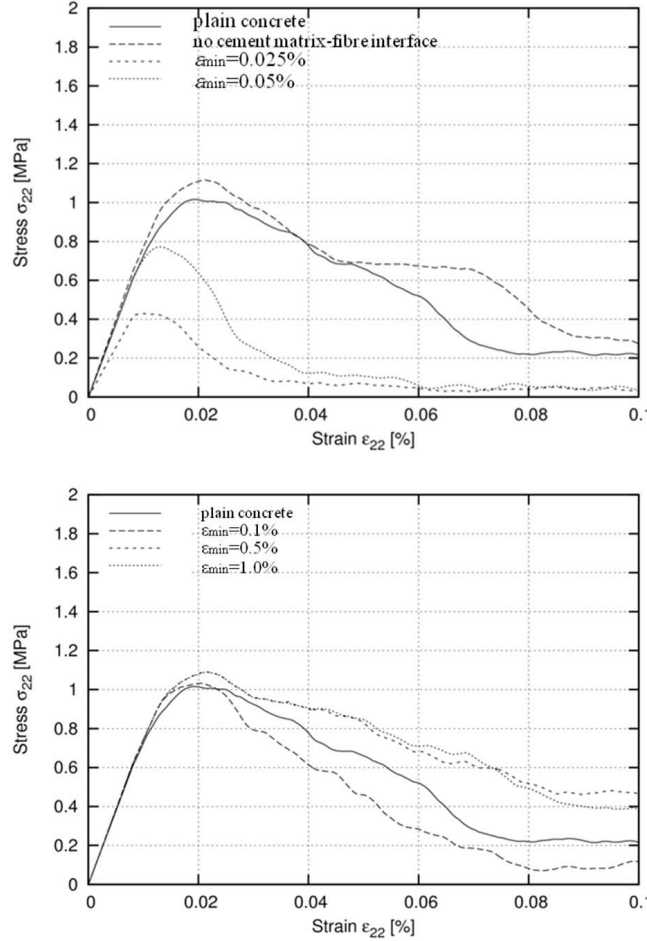
Fig. 8. Calculated stress-strain curve for 2D notched concrete specimen 5×5 cm^2, subjected to uniaxial extension with $A_f = 1.5\%$ area content of fibres for different threshold local strain $\varepsilon_{\min}$, in cement matrix-fibre interface (fibre length $l_f = 2$ cm) (σ_{22} – vertical normal stress, ε_{22} – vertical normal strain).
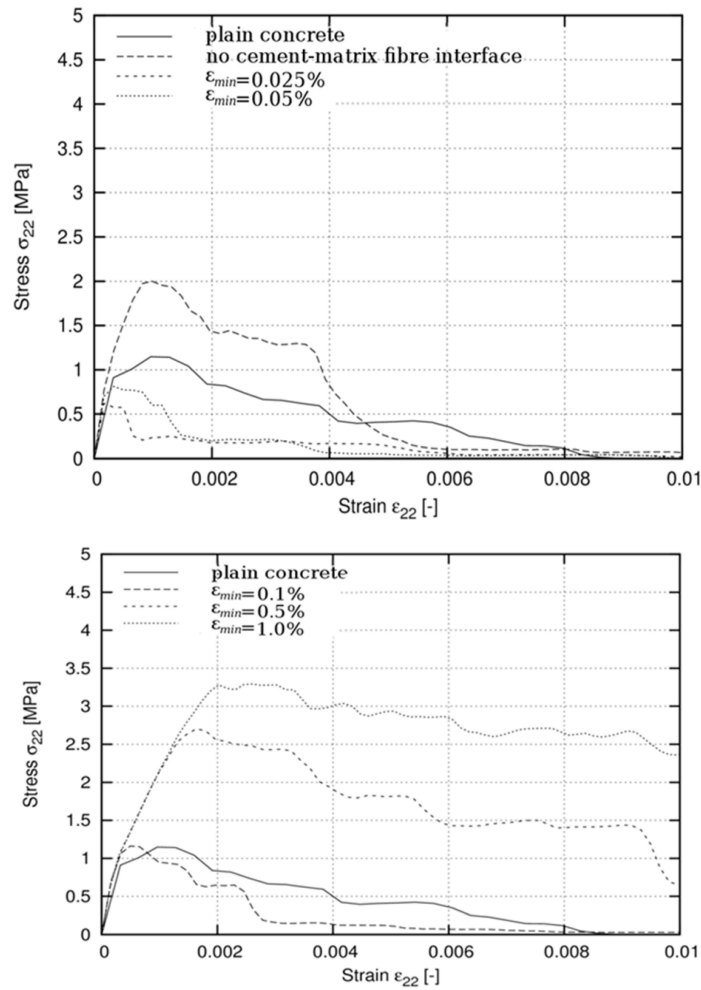
Fig. 9. Calculated stress-strain curve for 3D notched concrete specimen $5 \times 5 \times 5$ cm^3 subjected to uniaxial extension with $V_f = 1.5\%$ volume content of fibres for different threshold local strain $\varepsilon_{\min}$ in cement matrix-fibre interface (fibre length $l_f = 2$ cm) (σ_{22} – vertical normal stress, ε_{22} – vertical normal strain).

the same initial distribution of all concrete components. Figures 8 and 9 demonstrate the mean curves from 5 simulations. The development of the calculated fracture is shown in Figs. 10 and 11 (2D simulations) and in Fig. 12 (3D simulations) for 2 different specimen sizes (with $\varepsilon_{\min} = 0.5\%$ and $A_f = V_f = 1.5\%$).

Both the strength and ductility of fibrous concrete increase with increasing threshold local strain $\varepsilon_{\min}$ if the cement matrix-fibre interface is stronger than the cement matrix-aggregate interface, i.e. at $\varepsilon_{\min} \geq 0.5\%$ in the fibrous bond. This increase is very pronounced in 3D simulations. All further discrete simulations were carried out then with the threshold strain $\varepsilon_{\min} = 0.5\%$ in the cement
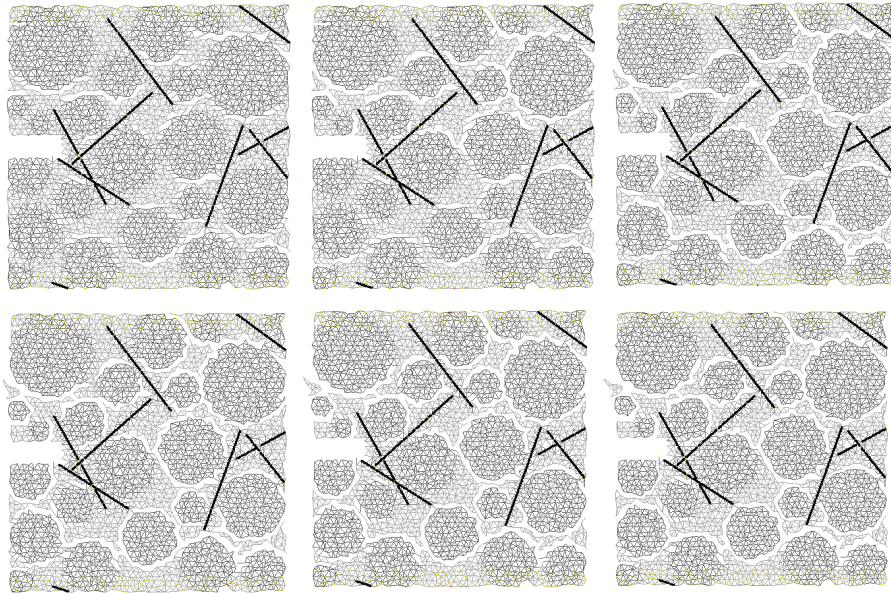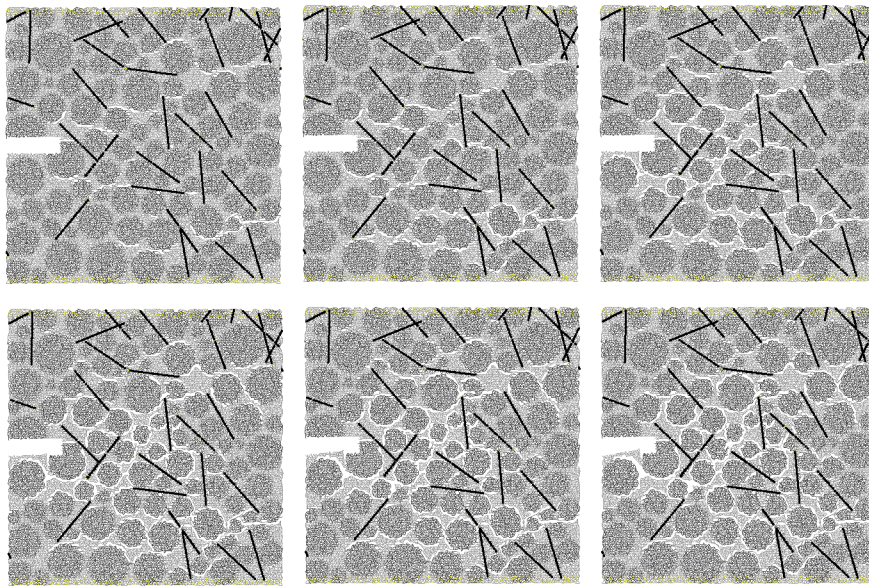
Fig. 10. Evolution of calculated crack pattern in 2D notched concrete specimen subjected to uniaxial extension: ($\varepsilon_{\min} = 0.5\%$, $l_f = 2$ cm, $A_f = 1.5\%$, $l_r = 1$ mm, specimen 5×5 cm^2, $\varepsilon_{\min}$ – threshold local tensile strain).
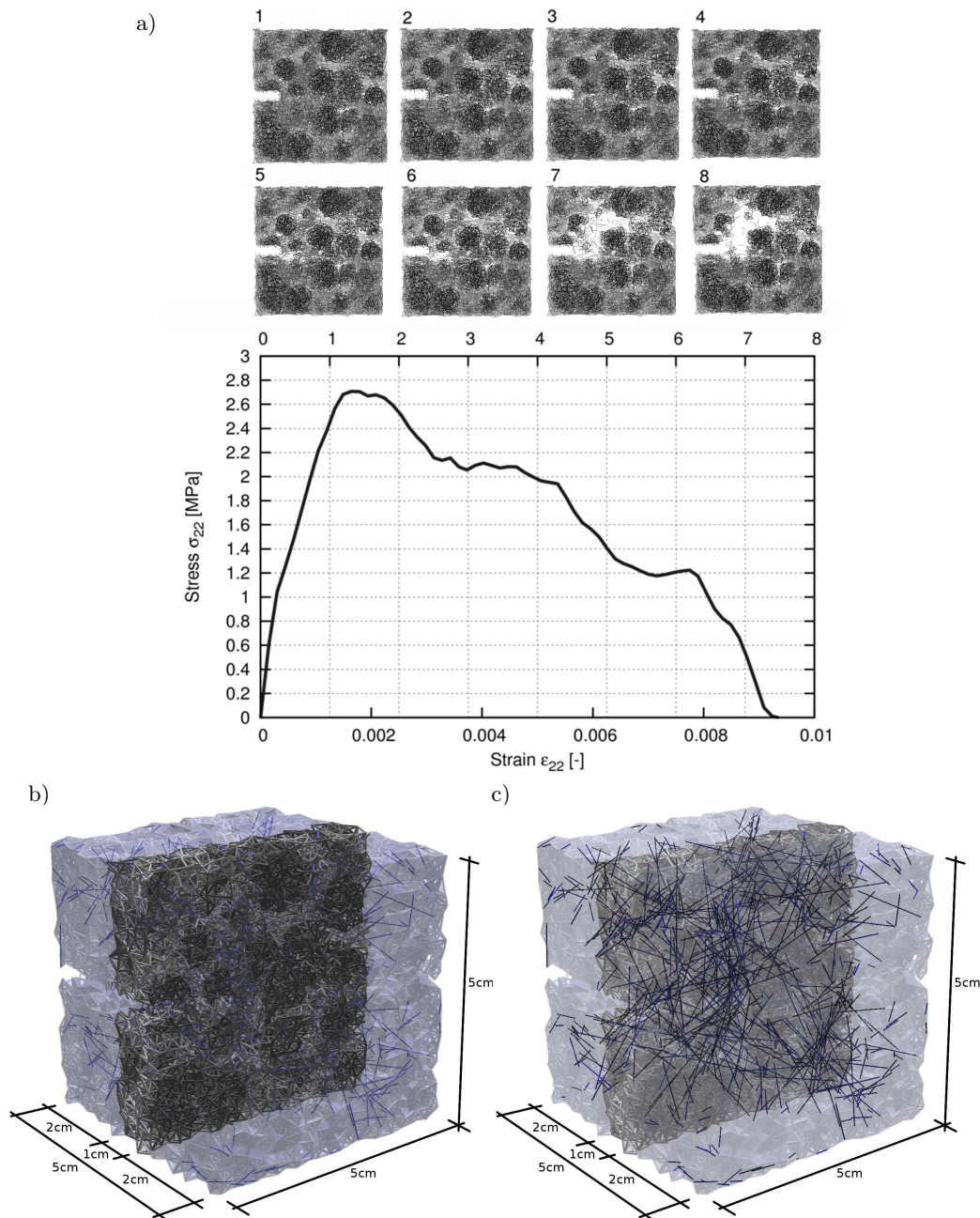

Fig. 11. Evolution of calculated crack pattern in 2D notched concrete specimen subjected to uniaxial extension: ($\varepsilon_{\min} = 0.5\%$, $l_f = 2$ cm, $A_f = 1.5\%$, $l_r = 1$ mm, specimen 10×10 cm^2, $\varepsilon_{\min}$ – threshold local tensile strain).

Fig. 12. Deformed specimen with crack pattern in notched concrete specimen $5 \times 5 \times 5$ cm^3 subjected to uniaxial extension: a) 2D deformation process in the mid-section of 1 cm thick in different stages (stage number given at the top), b) deformed 3D specimen with distinguished aggregates at peak (stage '1'), c) deformed 3D specimen with distinguished steel fibres at peak (stage '1'), (cement matrix-fibre interface with $\varepsilon_{\min}=0.5\%$, fibre volume $V_f=1.5\%$, $l_f=2$ cm, $l_r=2$ mm).

matrix-fibre interface. The calculated mean tensile strength of plain concrete
and fibrous concrete is 1.0 MPa and 1.1 MPa (2D simulations, $\varepsilon_{\min} = 0.5\%$) and
1.2 MPa and 2.6 MPa (3D simulations, $\varepsilon_{\min} = 0.5\%$), respectively. The fracture
energy is thus significantly higher in 3D simulations because: a) more fibres can
be placed in the volumetric unit than in the area unit with the same fibre length,
b) more rods break in 3D simulations what requires more fracture energy, c) the
crack propagation way is longer in 3D computations since the cracks are more
curved and propagate in a more tortuous manner, and d) torsion is taken into
account in 3D analyses. The vertical normal strain corresponding to the peak
on the stress-strain curve is also higher in 3D analyses: 0.02 (2D simulations)
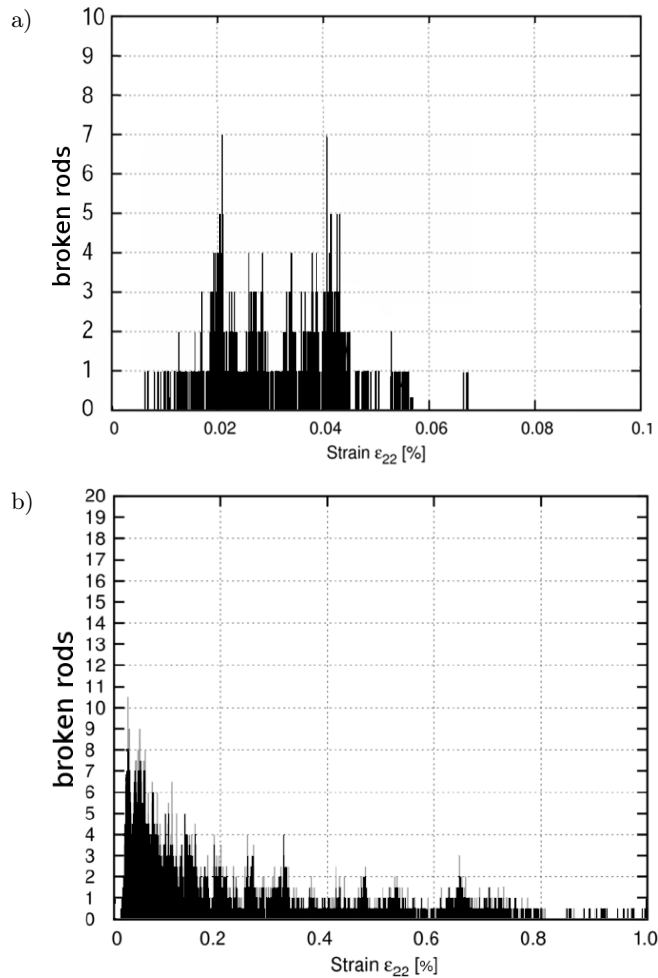and 0.002 (3D simulations) due to the different fracture formation. Figure 13

Fig. 13. Number of broken rods in each iteration during uniaxial extension for: a) 2D concrete
specimen and b) 3D concrete specimen.

compares the number of removed rods in each iteration during extension for 2D (with 8000 rods) and 3D simulations (with 170000 rods). It can be seen that significantly more rods break during 3D simulations of a fracture process (in particular at the onset of this process).

Due to a high particle density of 60% (Figs. 10–12), percolation of bond zones occurs early in the loading history. Since the interface between cement matrix and aggregate is the weakest component of the system, the material becomes initially weak there and cracks are created along the aggregate. The cracks are initiated in the region of the notch. Since the number of aggregates is relatively large, the cracks cannot propagate in long lines. Instead of this, several discontinuous macro-cracks propagate in a tortuous manner between fibres. The cracks overlap and form branches. The way propagation of cracks is clearly enhanced by the presence of steel fibres which delay their development.
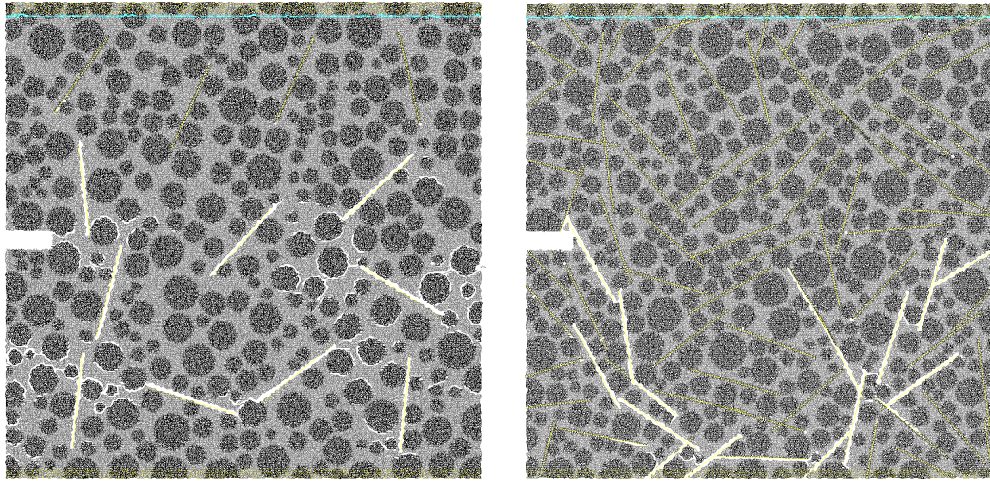

Fig. 14. Two 2D notched fibrous concrete specimens with steel fibres subjected to uniaxial extension: calculated crack pattern with cement matrix-fibre interface weaker than cement matrix-aggregate interface (case 'B' of Tab. 1).

If the cement matrix-fibre interface is weaker than the cement matrix-aggregate interface ($\varepsilon_{\min} < 0.05\%$), both the material strength and ductility are even smaller than in plain concrete due to the fact that cracks are created in interfaces along the fibres which act as strong imperfections to promote them (Fig. 14). In the case of lack of the cement matrix-fibre interface, both the material strength and ductility are also higher in fibrous concrete than in plain concrete (due to the different values of k_l and E, as compared to the cement matrix-aggregate interface, Table 1). However, the presence of the cement matrix-fibre interface with the different $\varepsilon_{\min}$ allows us to affect the evolution of the stress-strain curve.

3.2. Effect of fibre presence

The effect of fibres on the behavior of plain concrete is demonstrated for 2 different concrete specimen sizes ($\varepsilon_{\min} = 0.5\%$, $V_f = 1.5\%$, $A_f = 1.5\%$, $l_f = 2$ cm) in Figs. 15 (2D results) and 16 (3D results). Presented are three stress-strain curves: minimum, mean and maximum, on the basis of 5 simulations. Thus, a scatter of results around the mean value can be noticed.
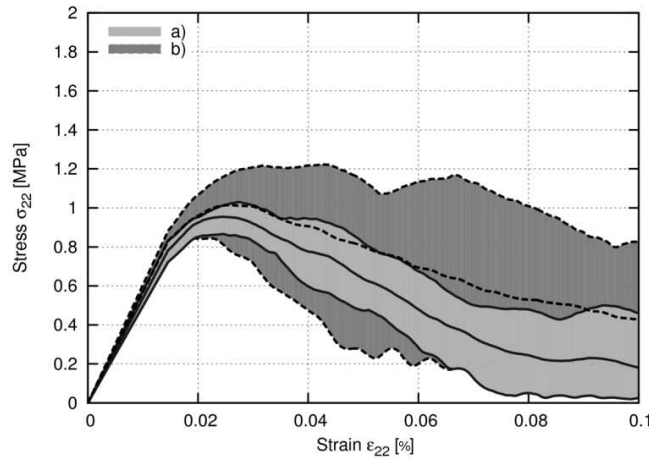

Fig. 15. Calculated stress-strain curves for 2D notched fibrous concrete specimens subjected to uniaxial extension ($\varepsilon_{\min} = 0.5\%$, $l_r = 1$ mm, specimen 5×5 cm^2): a) plain concrete, b) fibrous concrete with $A_f = 1.5\%$ and $l_f = 2$ cm (σ_{22} – vertical normal stress, ε_{22} – vertical normal strain, $\varepsilon_{\min}$ – threshold local tensile strain).
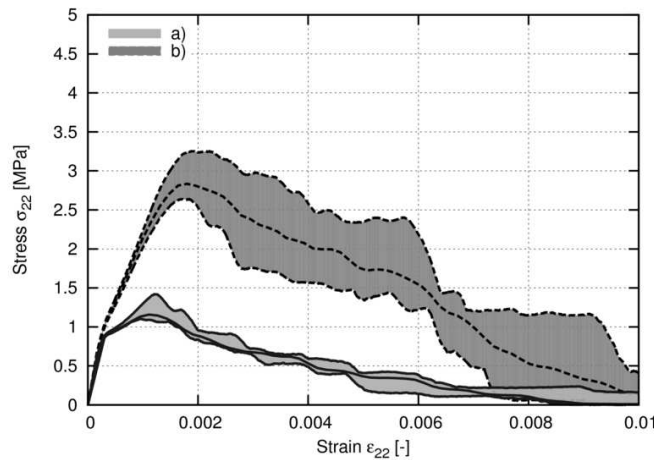

Fig. 16. Calculated stress-strain curves for 3D notched fibrous concrete subjected to uniaxial extension ($\varepsilon_{\min} = 0.5\%$, $l_r = 2$ mm, specimen $5 \times 5 \times 5$ cm^3): a) plain concrete, b) fibrous concrete with $V_f = 1.5\%$ and $l_f = 2$ cm (σ_{22} – vertical normal stress, ε_{22} – vertical normal strain, $\varepsilon_{\min}$ – threshold local tensile strain).

As in the experiments (SHAH and RANGAN [28], BENTUR and MINDESS [5]), both the concrete strength and ductility increase with fibres, depending strongly on their stochastic distribution. The tensile strength f_t improves from 0.85–1.0 MPa (plain concrete) up to 0.85–1.2 MPa (fibrous concrete) in 2D simulations, and from 1.1–1.4 MPa (plain concrete) up to 2.6–3.3 MPa (fibrous concrete) in 3D simulations. Thus, the scatter of results is higher in 3D analyses. The scatter is also higher in fibrous concrete than in plain concrete.

3.3. Effect of specimen size

The results of stress-strain curves during quasi-static uniaxial tension with fibrous concrete specimens with smooth horizontal edges are shown in Fig. 17 for the 2D specimens 5×5 cm^2 and 10×10 cm^2 ($\varepsilon_{\min} = 0.5\%$, $l_f = 1$ cm, $A_f = 1.5\%$),
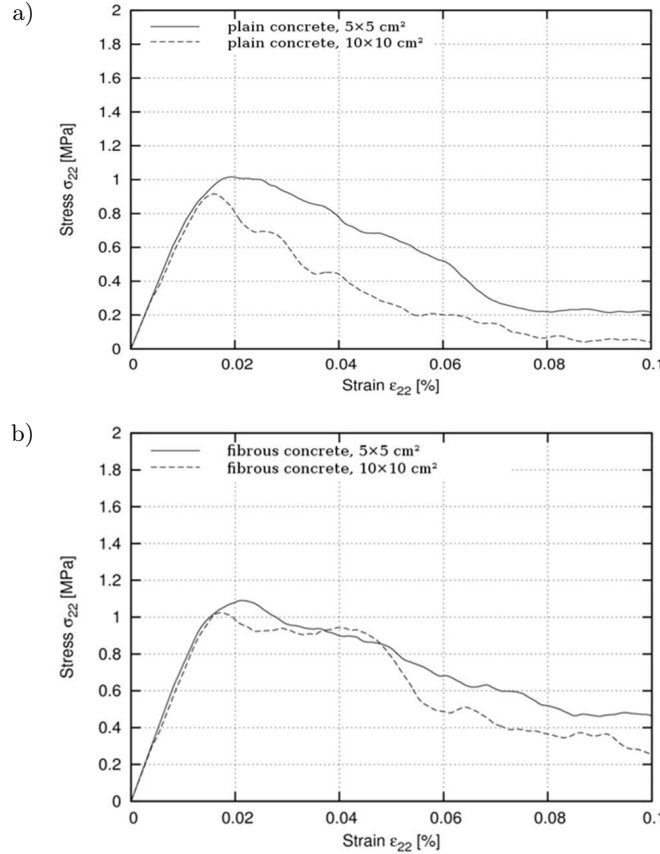

Fig. 17. Calculated stress-strain curves for 2D notched fibrous concrete specimens (5×5 cm^2 and 10×10 cm^2) subjected to uniaxial extension ($l_r = 1$ mm, $\varepsilon_{\min} = 0.5\%$), a) plain concrete, b) fibrous concrete with $A_f = 1.5\%$ and $l_f = 2$ cm (σ_{22} – vertical normal stress, ε_{22} – vertical normal strain).
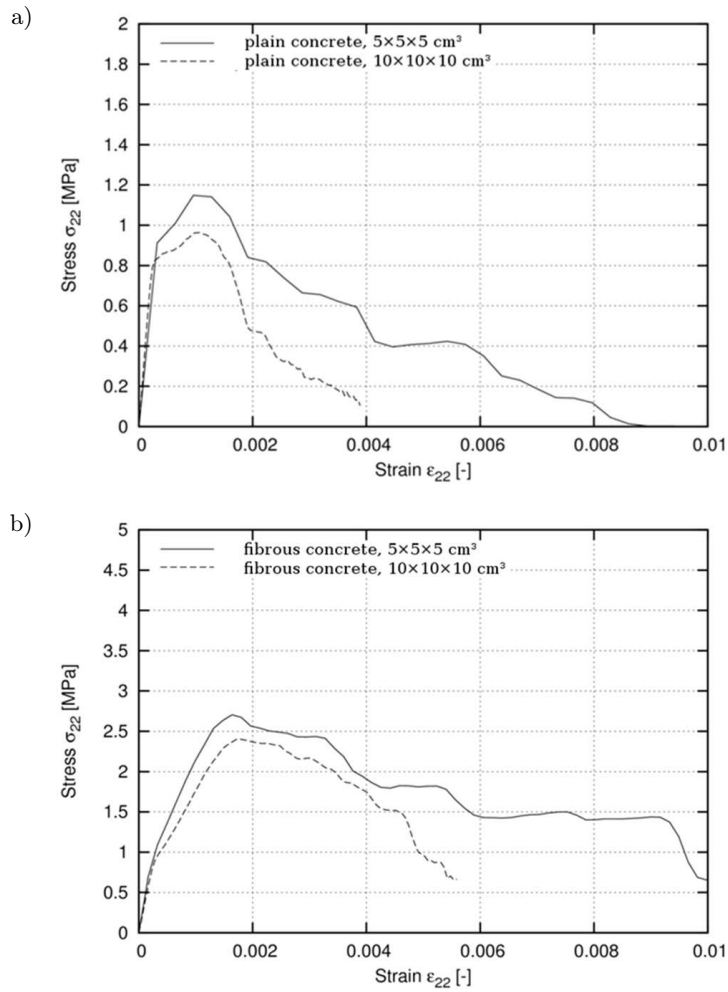
a)

b)

Fig. 18. Calculated stress-strain curves for 3D notched fibrous concrete specimens ($5 \times 5 \times 5$ cm^3 and $10 \times 10 \times 10$ cm^3) subjected to uniaxial extension ($l_r = 2$ mm, $\varepsilon_{\min} = 0.5\%$), a) plain concrete, b) fibrous concrete with $V_f = 1.5\%$ and $l_f = 2$ cm (σ_{22} – vertical normal stress, ε_{22} – vertical normal strain).

and in Fig. 18 for the 3D specimens $5 \times 5 \times 5$ cm^3 and $10 \times 10 \times 10$ cm^3 ($\varepsilon_{\min} = 0.5\%$, $l_f = 2$ cm, $V_f = 1.5\%$). Presented are the mean stress-strain curves only.

The results show that both the strength and ductility of plain and fibrous concrete are improved with decreasing specimen size. Thus, an experimental size effect is realistically modelled in 2D and 3D computations (Balendran [4], Ward and Li [37], Lin [22]). The size effect is stronger in a plain concrete specimen than in a fibrous one.

3.4. Effect of fibre orientation

Figures 19 and 20 show the effect of the direction and location of fibres in the smallest concrete specimen, which were distributed in the concrete specimen at random, vertically and horizontally, respectively. Five simulations were again performed for each case. Presented are the mean stress-strain curves only.
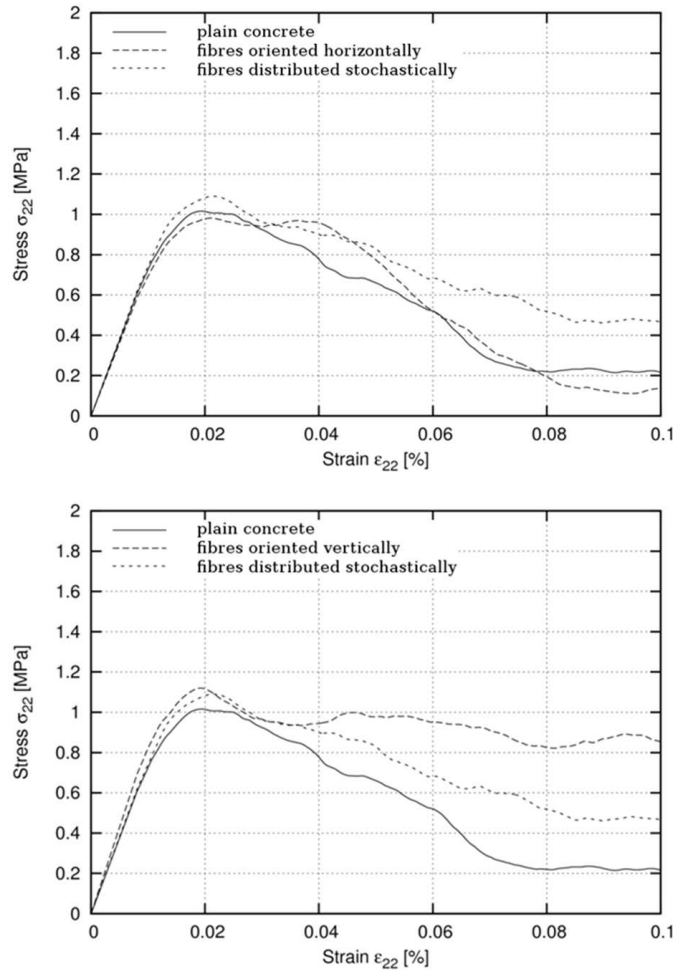

Fig. 19. Calculated stress-strain curves for 2D notched fibrous concrete specimens subjected to uniaxial extension ($\varepsilon_{\min} = 0.5\%$, specimen 5×5 cm^2, $l_r = 1$ mm) for plain concrete and fibrous concrete with different fibre orientation ($A_f = 1.5\%$, $l_f = 2$ cm) (σ_{22} – vertical normal stress, ε_{22} – vertical normal strain).

Similarly as in the experiments (LIN [22]), the concrete specimen becomes the strongest as compared to plain concrete when the fibres are oriented vertically, i.e. they are parallel to the loading direction (perpendicular to the direction
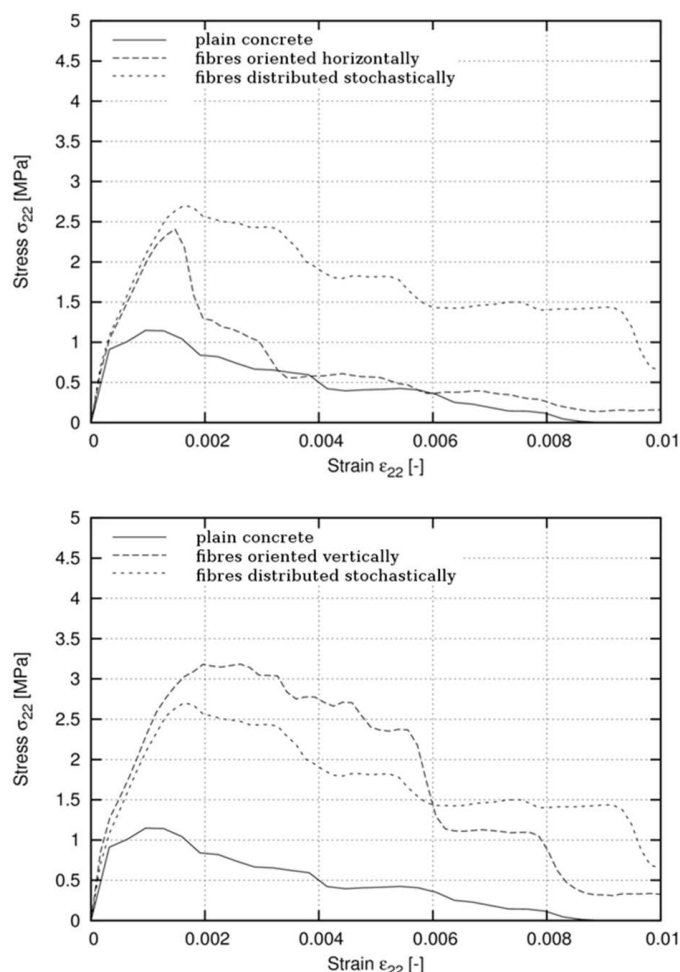
Fig. 20. Calculated stress-strain curves for 3D notched fibrous concrete specimens subjected to uniaxial extension ($\varepsilon_{\min} = 0.5\%$, specimen $5 \times 5 \times 5$ cm^3, $l_r = 2$ mm) for plain concrete and fibrous concrete with different fibre orientation ($V_f = 1.5\%$, $l_f = 2$ cm) (σ_{22} – vertical normal stress, ε_{22} – vertical normal strain).

of dominant horizontal cracks). The material becomes also the most ductile. In particular, the effect is pronounced in 3D analyses. The 3D fibrous specimen is stronger by 25% if the fibres are vertically oriented, and weaker by 10% if the fibres are horizontally oriented, as compared to a mean stochastic tensile strength $f_r = 2.6$ MPa (at $V_f = 1.5\%$). If the fibres are horizontally oriented, the strength's increase, as compared to plain concrete, is by 100%, and if the fibres are vertically oriented, the strength's growth as compared to plain concrete is 200% (at $V_f = 1.5\%$). The fibre orientation effect in 2D simulations is significantly weaker.

3.5. Effect of fibre length

The effect of the fibre length on the stress-strain curve during uniaxial tension is demonstrated in Figs. 21 and 22, in 2 different fibrous concrete specimens. The fibre length was 1–6 cm (threshold strain $\varepsilon_{\min} = 0.5\%$ in the cement matrix-fibre interface).

In 3D simulations, concrete strength and ductility increase with increasing fibre length independently of the specimen size as in experiments (WARD and LI [37]). However, this does not occur in 2D calculations where the effect of a tochastic distribution of fibres can be stronger.
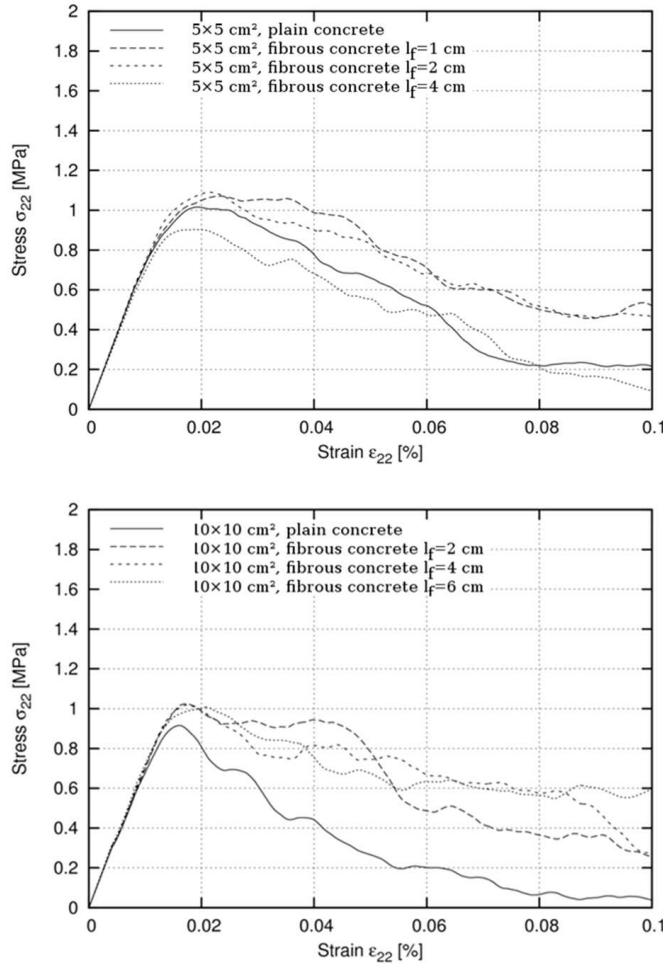

Fig. 21. Calculated stress-strain curves for 2D notched concrete specimens (5×5 cm^2 and 10×10 cm^2) subjected to uniaxial extension ($\varepsilon_{\min} = 0.5\%$, $l_r = 1$ mm) for plain concrete and fibrous concrete with different fibre lengths l_f ($A_f = 1.5\%$) (σ_{22} – vertical normal stress, ε_{22} – vertical normal strain).

Fig. 22. Calculated stress-strain curves for 3D notched concrete specimens ($5 \times 5 \times 5$ cm^3 and $10 \times 10 \times 10$ cm^3) subjected to uniaxial extension ($\varepsilon_{\min} = 0.5\%$, $l_r = 2$ mm) for plain concrete and fibrous concrete with different fibre lengths l_f ($V_f = 1.5\%$) (σ_{22} – vertical normal stress, ε_{22} – vertical normal strain).
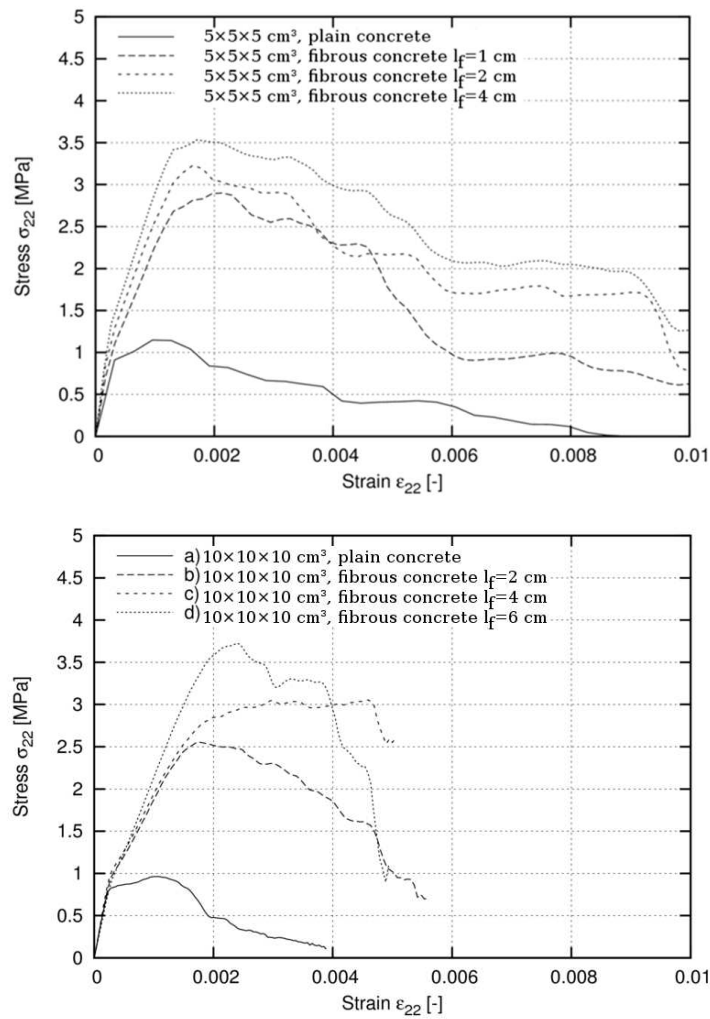
3.6. Effect of torsion in 3D simulations

The 3D results with a plain concrete and a fibrous concrete specimen ($V_f = 1.5\%$, $l_f = 2$ cm) are demonstrated in Fig. 23. One assumed the stiffness parameter k_t=0 or $k_t = k_b$ (k_t – torsional stiffness parameter, k_b – bending stiffness parameter). The strength is obviously higher when the torsional stiffness is taken into account.
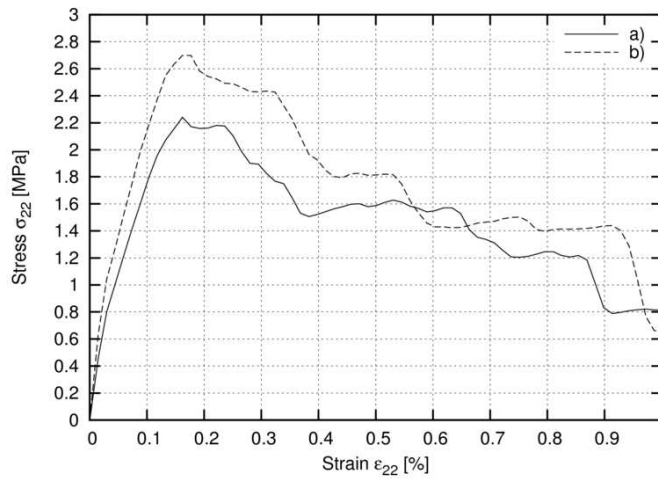
Fig. 23. Calculated stress-strain curves for 3D notched fibrous concrete specimens subjected to uniaxial extension ($\varepsilon_{\min} = 0.5\%$, $l_r = 2$ mm, specimen $5 \times 5 \times 5$ cm^3): a) $k_t = 0$, b) $k_t = k_b$ ($V_f = 1.5\%$, $l_f = 2$ cm) (σ_{22} – vertical normal stress, ε_{22} – vertical normal strain, k_t – torsional stiffness parameter and k_b – bending stiffness parameter).

4. Conclusions

In this paper, a novel simulation framework was used to study fracture in fibrous concrete specimens where individual steel fibres were explicitly modeled in the irregular lattice. The innovative points were following: a) the fracture process in 3D fibrous concrete was simulated (which has not been sufficiently studied in the literature), b) the cement matrix-fibre interface was considered in simulations, and c) the effect of the fibre orientation on the stress-strain curve was investigated (which is the most important parameter when designing the fibrous concrete). The following conclusions can be drawn from numerical calculations.

The lattice model, in spite of its simplicity, is capable of simulating fracture in plain and fibrous concrete. The obtained results of crack patterns and stress-strain curves for fibrous concrete during uniaxial tension, compare qualitatively well with experimental results. By using an elastic-purely brittle local fracture law at the particle level of the material, global softening behavior is obtained.

The heterogeneous 3D lattice model for fibrous concrete used in the paper requires five material parameters for each of 3 phases (cement matrix, aggregate, fibres) and 2 interfaces (cement matrix-fibre interface, cement matrix-aggregate interface) and 2 grid parameters related to the distribution of rod elements. The advantage of our quasi-static lattice model is due to its explicit character. Thus, a large number of elements could be taken into account when using parallelized computers.

The strength and ductility of fibrous concrete specimens are improved with increasing strength of cement matrix-fibre bond during uniaxial extension, if the strength of cement matrix-fibre interfaces is higher than the strength of cement matrix-aggregate interfacial zones. In this case, the crack propagation is delayed by the presence of steel fibres.

The orientation of fibres strongly influences strength and failure of the material. The effectiveness of fibrous concrete significantly improves if fibres are located perpendicularly to the cracks' direction.

The strength and ductility of fibrous concrete specimens increase with increasing fibre length.

A deterministic size effect occurs in fibrous concrete specimens, i.e. the strength and ductility increase with decreasing specimen size. It is weaker than in plain concrete specimens.

The material behavior in the 3D model is significantly stronger and more ductile than in the 2D model using the same material parameters. In addition, the maximum vertical normal strain corresponding to strength is significantly larger in 3D simulations. A scatter of results is also higher in 3D simulations. A scatter is also higher in fibrous concrete than in plain concrete.

The calculations with a lattice model will be continued. Further calibration studies will be performed by taking into account the real heterogeneous microstructure of fibrous concrete specimens. The possibility of a crack closure during compression will be considered. A two-scale approach will be used linking the lattice model with the continuum elastic-plastic model, wherein the first model will be only restricted to the damaged and fractured part of the specimen. In addition, inertial forces will be taken into account during dynamic calculations.

Acknowledgment

References

1. S.A. Al-Taan, N.A. Ezzadeen, *Flexural analysis of reinforced fibrous concrete members using the finite element method*, Computers and Structures, **56**, 6, 1065–1072, 1995.

2. F. Altun, T. Haktanir, K. Ari, *Effects of steel fiber addition on mechanical properties of concrete and RC beams*, Construction and Building Materials, **21**, 3, 654–662, 2007.

3. P. Balaguru, S.P. Shah, *Fiber reinforced cement composites*, McGraw Hill, 1992.

4. R.V. Balendran, F.P. Zhou, A. Nadeem, A.Y.T. Leung, *Influence of steel fibres on strength and ductility of normal and lightweight high strength concrete*, Building and Environment, **37**, 1361–1367, 2002.

5. A. Bentur, S. Mindess, *Fiber reinforced cementitious composites*, Elsevier Applied Science, New York, 1990.

6. J.E. Bolander, S. Saito, *Discrete modeling of short-fiber reinforcement in cementitious composites*, Adv. Cem. Based Mater., **6**, 76–86, 1997.

7. H. Chenkui, Z. Guofan, *Properties of steel fibre reinforced concrete containing larger coarse aggregate*, Cement and Concrete Composites, **17**, 199–206, 1995.

8. G. Cusatis, Z.P. Bazant, L. Cedolin, *Confinement-shear lattice model for concrete damage in tension and compression: I. Theory*, ASCE Journal of Engineering Mechanics, **129**, 12, 1439–1448, 2003.

9. S. Eckardt, C. Könke, *Simulation of damage in concrete structures using multiscale models. Computational Modelling of Concrete Structures*, EURO-C, G. Meschke, R. de Borst, H. Mang, N. Bicanic (Eds.), Taylor and Francis, 77–83, 2006.

10. H. Falkner, V. Henke, *Stahlfaserbeton- konstruktive Anwendungen*, Beton- und Stahlbetonbau, **95**, 10, 597–606, 2000.

11. P.A. Jones, S.A. Austin, P.J. Robins, *Predicting the flexural load-deflection response of steel fibre reinforced concrete from strain, crack-width, fibre pull-out and distribution data*, Materials and Structures, **41**, 449–463, 2008.

12. P. Kabele, *Multiscale framework for modeling of fracture in high performance fiber reinforced cementitious composites*, Engineering Fracture Mechanics, **74**, 194–209, 2007.

13. K. Komlos, B. Babal, T. Nürnbergerova, *Hybrid fibre-reinforced concrete under repeated loading*, Nuclear Enginering and Design, **156**, 195–200, 1995.

14. A.G. Kooiman, C. van der Veen, J. C. Walraven, *Design Relation for Steel Fibre Reinforced Concrete*, Heron, **45**, 275–307, 2000.

15. J. Kozicki, *Application of discrete models to describe fracture process in brittle materials*, Phd Thesis, University of Gdańsk, Poland, 2007.

16. J. Kozicki, J. Tejchman, *Effect of aggregate structure on fracture process in concrete using 2D lattice model*, Archives of Mechanics, **59**, 4–5, 1–20, 2007.

17. J. Kozicki, J. Tejchman, *Modelling of fracture processes in concrete using a novel lattice model*, Granular Matter, **10**, 5, 399–405, 2008.

18. J. Kozicki, F.V. Donze, *A new open-source software developed for numerical simulations using discrete modeling methods*, Computer Methods in Applied Mechanics and Engineering, **197**, 4429–4443, 2008.

19. N. Krstulovic-Opara, A.R. Haghayeghi, M. Haidar, P.D. Krauss, *Use of conventional and high-performance steel-fiber reinforced concrete for bridge deck overlays*, ACI Mater J., **92**, 6, 669–677, 1995.

20. V.C. Li, H. Horii, P. Kabele, T. Kanda, Y.M. Lim, *Repair and retrofit with engineered cementitious composites*, Engineering Fracture Mechanics, **65**, 317–334, 2000.

21. Z. Li, M.A. Perez Lara, J.E. Bolander, *Restraining effects of fibers during non-uniform drying of cement composites*, Cement and Concrete Research, **36**, 1643–1652, 2006.

22. Y.Z. Lin, *Tragverhalten von Stahlfaserbeton*, Deutscher Ausschuss für Stahlbeton, Heft 494, Berlin, Beuth Verlag GmbH, 1999.

23. T.Y. Lim, P. Paramaivam, S.L. Lee, *Analytical model for tensile behaviour of steel-fibre concrete*, ACI Materials Journal, 1987.

24. Y. Mohammadi, S.P. Singh, S.K. Kaushik, *Properties of steel fibrous in fresh and hardened state*, Construction and Building Materials, **22**, 956–965, 2008.

25. F. Radtke, A. Simone, L.J. Sluys, *A computational model for failure in fibre reinforced concrete including the influence of discrete fibre distributions*, Proc. 1th Int. Conf. "Computational Technologies in Concrete Structures" CTCS'09, 767–781, 2009a.

26. F. Radtke, A. Simone, L.J. Sluys, *A computational model for failure analysis of fibre reinforced concrete with discrete treatment of fibres*, Engng. Fracture Mech., **77**, 4, 597–620, 2010.

27. C. Redon, J.-L. Chermant, *Damage mechanics applied to concrete reinforced with amortphous cast iron fibers, concrete subjected to compression*, Cement and Concrete Composites, 21, 197–204, 1999.

28. S.P. Shah, B.V. Rangan, *Fiber reinforced concrete properties*, ACI Journal, **68**, 2, 126–135, 1971.

29. E. Schlangen, E.J. Garboczi, *Fracture simulations of concrete using lattice models: computational aspects*, Engineering Fracture Mechanics, **57**, 319–332, 1997.

30. B. Schnütgen, M. Teutsch, *Beonbauwerke aus Stahlfaserbeton beim Umgang mit umweltgefährdenden Stoffen*, Beton- und Stahlbetonbau, **96**, 7, 451–457, 2001.

31. D.V. Soulioti, N.M. Barkoula, A. Paipetis, T.E. Matikas, *Effects of fibre geometry and volume fraction on the flexural behaviour of steel-fibre reinforced concrete*, Strain, DOI 10.1111/j.1475-1305.2009.00652.x.

32. J. Tejchman, J. Kozicki, *Steel-fibrous concrete – experiments and a numerical discrete model*, University of Gdańsk Publishers, 2009.

33. J.G.M. van Mier, E. Schlangen, A. Vervuurt, *Lattice type fracture models for concrete*, Continuum Models for Materials with Microstructure, H.B. Mühlhaus [Ed.], John Wiley & Sons, 341–377, 1995.

34. A. van Hauwaert, J.G.M. van Mier, *Computational modeling of the fibre-matrix bond in steel fibre reinforced concrete*, Fracture Mechanics of Concrete Structures, H. Mihashi, K. Rokugo [Eds.], Aedificatio Publishers, Freiburg, Germany, 561–571, 1998.

35. J.G.M. van Mier, M.R.A. van Vliet, *Influence of microstructure of concrete on size/scale effects in tensile fracture*, Engineering Fracture Mechanics, **70**, 16, 2281–2306, 2003.

36. J.C. Walraven, S. Grünewald, *Regelung und Anwendung des Stahlfaserbetons in den Niederlanden. Stahlfaserbeton – ein unberechenbares Material?*, Bauseminar 2002, Braunschweig, **164**, 47–63, 2002.

37. R.J. Ward, V.C. Li, *Dependence of flexural behavior of fiber reinforced mortar on material fracture resistance and beam size*, ACI Materials Journals, 1990.

38. R.F. Zollo, *Fiber-reinforced concrete: an overview after 30 years of development*, Cement Concrete Compos., **19**, 2, 107–122, 1997.